Synchronous Ensembles of Hippocampal CA1 Pyramidal Neurons Associated with Theta but not Ripple Oscillations During Novel Exploration

En-Li Chen[1,2], Tsai-Wen Chen[1,2], Eric R. Schreiter[3], Bei-Jung Lin[1,2*]

[1]Institute of Neuroscience, National Yang Ming Chiao Tung University, Taipei, Taiwan
[2]Brain Research Center, National Yang Ming Chiao Tung University, Taipei, Taiwan
[3]Janelia Research Campus, Howard Hughes Medical Institute, Ashburn, VA 20147, USA.
*Corresponding author: beijunglin@nycu.edu.tw

Abstract

Synchronous neuronal ensembles play a pivotal role in the consolidation of long-term memory in the hippocampus. However, their organization during the acquisition of spatial memory remains less clear. In this study, we used neuronal population voltage imaging to investigate the synchronization patterns of CA1 pyramidal neuronal ensembles during the exploration of a new environment, a critical phase for spatial memory acquisition. We found synchronous ensembles comprising approximately 40% of CA1 pyramidal neurons, firing simultaneously in brief windows (~25ms) during immobility and locomotion in novel exploration. Notably, these synchronous ensembles were not associated with ripple oscillations but were instead phase-locked to local field potential theta waves. Specifically, the subthreshold membrane potentials of neurons exhibited coherent theta oscillations with a depolarizing peak at the moment of synchrony. Among newly formed place cells, pairs with more robust synchronization during locomotion displayed more distinct place-specific activities. These findings underscore the role of synchronous ensembles in coordinating place cells of different place fields.

Introduction

The establishment of long-term memory involves the initial acquisition and subsequent consolidation of memory traces, processes intricately connected to the modification of synaptic transmission[1,2]. Synchronous ensembles, characterized by the simultaneous firing of multiple neurons over tens of milliseconds (referred to as population synchrony), play a pivotal role in influencing synaptic plasticity[3-5]. The hippocampus, a crucial region for long-term memory formation[6,7], has been a focal point of synchronous ensemble studies. Within the hippocampus, synchronous ensembles are hypothesized to play roles in reactivating and consolidating labile memory traces[8]. However, their organization during memory acquisition remains less understood.

In the hippocampus, synchronous ensembles among CA1 pyramidal cells (CA1PCs) are predominantly observed during sharp-wave ripples, the brain waves associated with memory consolidation[8-13]. During these events, 10-18% of CA1PCs generate spikes, particularly during offline consummatory behavioral states or sleep[14,15]. These synchronous ensembles are biased toward experience-dependent reactivation, consolidating labile memory traces[16,17]. Furthermore, synchronous ensembles firing action potentials in short windows of 10-30 milliseconds enhance information processing[6] and discriminate distinct behavioral contingencies[18]. Although synchronous ensembles of CA1PCs during offline memory consolidation are well-characterized, their organization during online acquisition of spatial memory, such as when animals enter a new environment and new place cells form, remains unclear.

Previous studies have identified correlated activities among place cells during theta oscillation, where 1-3% of place cells' spikes co-activate in a forward order matching animals' trajectory in the theta cycles when animals' locations overlap in the place fields of these cells[19-21]. Because these place cells fire at distinct theta phases in the same cycle, this coordinated firing operates on the timescale of theta periods (~125ms)[22,23]. Population synchrony on shorter timescales (10-30 ms) is

53 speculated to be reduced by the presence of theta oscillations[22].

54

55 The subthreshold membrane voltage (subVm), influenced by synaptic inputs and intrinsic
56 conductances, directly triggers spiking activity[24,25]. Additionally, properties of subVm support the
57 organization of neuronal representation[26]. Although correlated membrane potentials have been
58 proposed to underlie the synchrony of neuronal ensembles[27,28], multicellular recordings of subVms
59 have not yet provided direct experimental evidence. Given the intricate interaction among subVm,
60 spiking, and place cell formation, it is crucial to investigate the temporal relationships of sub- and
61 suprathreshold neuronal activities among CA1PCs during novel exploration.

62

63 In this study, we used voltage imaging to investigate the temporal dynamics of sub- and
64 suprathreshold neuronal activities in CA1PCs during novel exploration. We found synchronous
65 ensembles involving approximately 40% of CA1PCs exhibited transient population synchrony and
66 correlated subthreshold membrane potentials when mice ran and stopped in a new maze.
67 Surprisingly, these synchronous ensembles occurred outside ripple episodes and were phase-locked
68 to extracellular and intracellular theta oscillations. Notably, cell pairs with stronger synchronous
69 activities established more distinct place fields that overlapped less. In essence, synchronous
70 ensembles facilitated temporal association among place cells representing diverse features of
71 spatial memory. This plastic network, driven by synchronous ensembles, may contribute to the
72 stabilization of place cells, establishing place fields that effectively tile the environment.

73

74 Results

75 To investigate the temporal relationships between neuronal activities during novel exploration, we
76 simultaneously recorded many neurons as animals explored a new environment for the first time.
77 To achieve this, we employed voltage imaging in conjunction with an air-lifted plastic track that
78 allowed mice to explore an environment while remaining head-fixed under a microscope (Fig. 1A).

To ensure a genuinely novel experience, all pre-training and habituation were performed in a separate room distinct from the one where the imaging experiments were conducted. On the day of imaging, the mice were introduced to the recording room for the first time and initially confined to a specific corner of the track (Fig. 1A top view). Subsequently, as the imaging session commenced, the confinement was lifted, granting mice the freedom to explore the track while imaging was conducted.

In novel exploration, mice moved at a speed of 8.3±0.9 cm/s during locomotion (speed>3 cm/s) and spent 53±7% and 36±6% of their time in locomotion and immobility (speed<1 cm/s), respectively (n=5 mice). Meanwhile, they completed 10±2.5 laps during the 180-s imaging periods (n=5 mice).

For voltage imaging, we expressed the voltage indicator Voltron2[29] in CA1 pyramidal cells (CA1PCs), allowing us to measure both suprathreshold and subthreshold membrane potentials from multiple CA1PCs (14±4 cells imaged per field of view (mean±s.d.) and, in total, 71 cells imaged from 5 fields of view in 5 mice; Fig. 1B). Simultaneously, we monitored the animals' positions and speed within the track while recording the local field potential (LFP) from the contralateral side of the hippocampus.

The mean firing rates of cells ranged from 2.3 to 4.3 Hz (25th-75th percentiles) with a median of 3.2 Hz (n=71 cells, Fig. S1A). Additionally, most CA1PCs exhibited elevated mean firing rates during immobility relative to locomotion, and their firing rates showed a negative correlation with the animals' speed (Fig. S1B and S1C), consistent with previous research[30].

Synchronous ensembles among many CA1 pyramidal neurons

Figure 1C shows the fluorescence traces of all neurons in a session as an example. Instances of synchronous activity, where many neurons emitted spikes within a narrow time window, were frequently observed (Fig. 1C). To investigate synchronous activity within the neuronal population,

we selected a reference cell and counted the number of spikes across all other cells that were aligned with the spikes of the reference cell. This approach yielded a grand average cross-correlogram (CCG) capable of elucidating the timing of spikes from the reference cell relative to the combined spikes of the rest of the population. Notably, the grand average CCG exhibited heightened spike counts around zero lags, unlike flattened counts calculated from randomly selected cells of different sessions (Fig. 1D and 1E). The full width at half maximum (FWHM) of the peak in the grand average CCG measured 23±14 ms (mean±s.d., n=71 cells from 5 sessions; Fig. 1F), indicating the timescale of the population synchrony. Furthermore, pairwise CCGs of many cell pairs showed significant peaks compared to jittered data (percentage of significant pairs: 63%, median, n=497 pairs, Fig. S2A and S2B). Among pairs with significant peaks, the absolute values of the peak lags ranged from 0.8 to 4.3 ms (25th-75th percentiles) with a median of 2.1 ms, and the FWHM of the peaks ranged from 20 to 46 ms (25th-75th percentiles) with a median of 30 ms (n=315 pairs, Fig. S2C and S2D). These results highlight the synchronous spiking between neurons on the millisecond timescale.

To systematically reveal individual synchronous events, we counted the number of spikes from all simultaneously recorded neurons within sliding windows of 25 ms. To compare the summed spikes with controls, we randomly jittered the spike trains to perturb spike timings while maintaining spike rates. We identified moments of population synchrony when spike sums exceeded the average of the jittered spike sums plus four standard deviations (Fig. 1C). Using the same criterion for event detection, we observed over a 7.8-fold increase in synchronous events in original data compared to jittered controls (mean event rate: 0.94±0.17 Hz for the original data, 0.12±0.01 Hz for the jittered data, n=10 segments, p=0.002, Wilcoxon signed-rank test; Fig. 1G). Furthermore, we calculated the percentage of neurons participating in these synchronous events to examine the synchronous ensemble sizes. The ensemble sizes ranged from 32% to 53% (25th-75th percentiles) with a median of 42%, which were larger than the synchronous ensemble sizes associated with ripples[14] (Fig. 1H).

132 These results demonstrate synchronous ensembles of CA1PCs engaging many neurons.

133

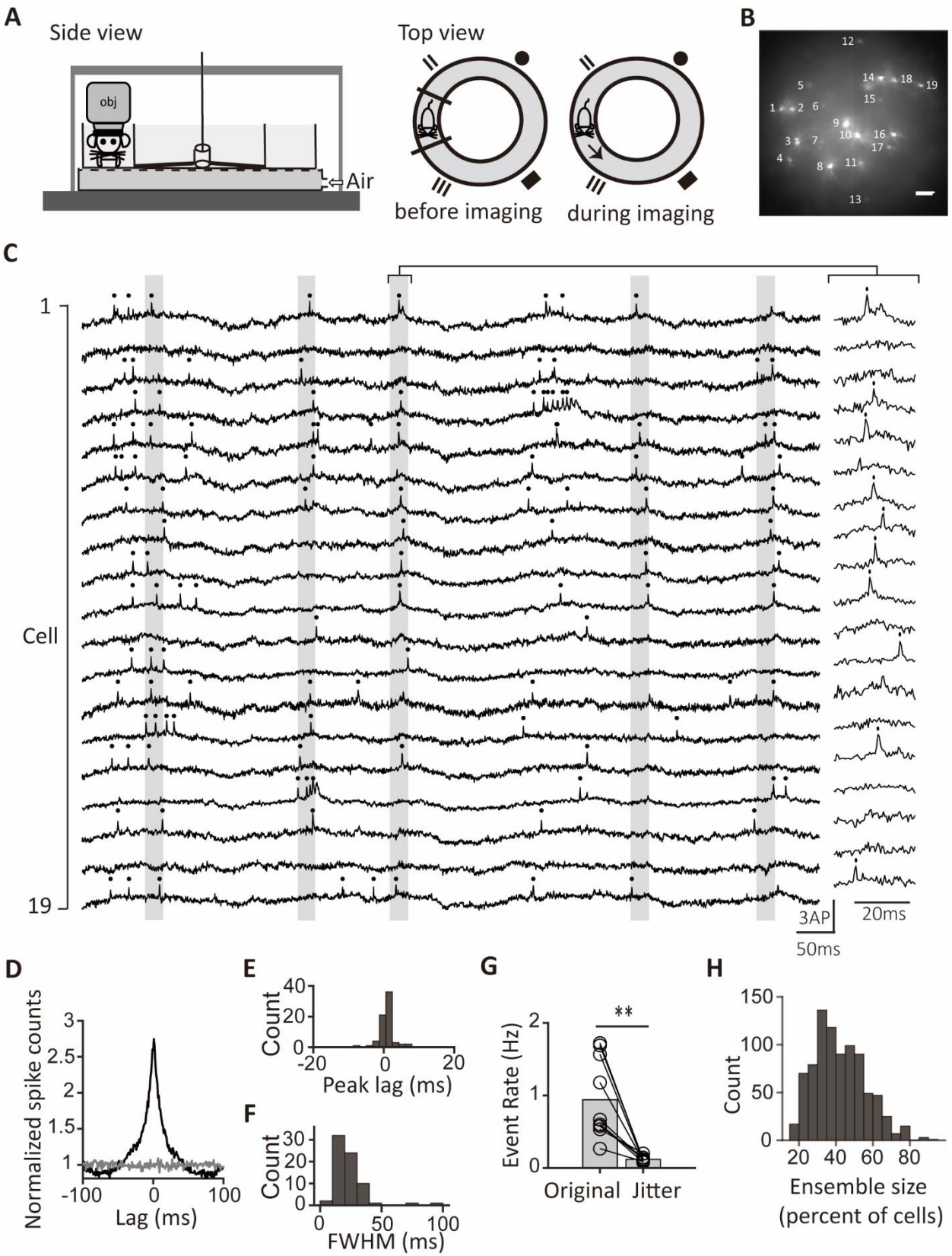

134

135 **Figure 1 Population synchrony during novel exploration.**

136 **(A)** Schematic of the behavioral setup for voltage imaging. Mice explored a novel one-way track
137 while fluorescence images were captured at the CA1 pyramidal layer. Left: side view; right: top view
138 of the setup.
139 **(B)** Example time-averaged image of CA1 pyramidal cells expressing Voltron2-ST labeled with JF_{552}-
140 HaloTag ligand. Scale bar, 100 μm.
141 **(C)** Fluorescence traces of cells in an example session with identified synchronous ensembles (gray
142 rectangles). Right: an example of magnified fluorescence traces within the bracket, pinpointing the
143 occurrence of the identified synchronous ensemble. Spikes are indicated by dots on the top.
144 **(D)** The grand average cross-correlogram (CCG) averaged across all 71 cells. The gray line represents
145 the mean grand average CCG between reference cells and randomly selected cells from different
146 sessions.
147 **(E)** Distribution of the grand average CCG peak lags of all cells (n=71).
148 **(F)** Distribution of the full width at half maximum (FWHM) of the grand average CCGs (n=71 cells).
149 **(G)** Pairwise comparison of the event rates of population synchrony between original and jittered
150 data. Bar heights indicate group means. **p<0.01
151 (**H**) Histogram of the ensemble sizes as percentages of cells participating in the synchronous
152 ensembles.
153
154
155 **Synchronous ensembles during locomotion and immobility of novel exploration**
156 The hippocampus exhibits state-dependent activities when rodents are engaged in locomotion and
157 immobility[30,31]. In novel exploration, CA1PCs showed synchronous spiking during locomotion and
158 immobility (Fig. 2A). To investigate whether these synchronous activities differed between these
159 behavioral states, we compared grant average CCGs and synchronous ensembles under these
160 conditions. During both immobility and locomotion, grant average CCGs showed prominent peaks
161 compared to jittered data (Fig. 2B). Moreover, synchronous ensembles were rich in both immobility

162 and locomotion periods (Fig. 2A, B, and D). Nevertheless, the FWHMs of grant average CCGs were
163 broader in the immobility group compared to the locomotion group (Fig. 2B and C). Synchronous
164 events occurred more frequently during immobility compared to locomotion (Fig. 2D). Additionally,
165 ensemble sizes were significantly larger in the immobility group compared to the locomotion group
166 (Fig. 2E). Taken together, with differences in sizes and kinetics, there were synchronous ensembles
167 during both immobility and locomotion periods of novel exploration.

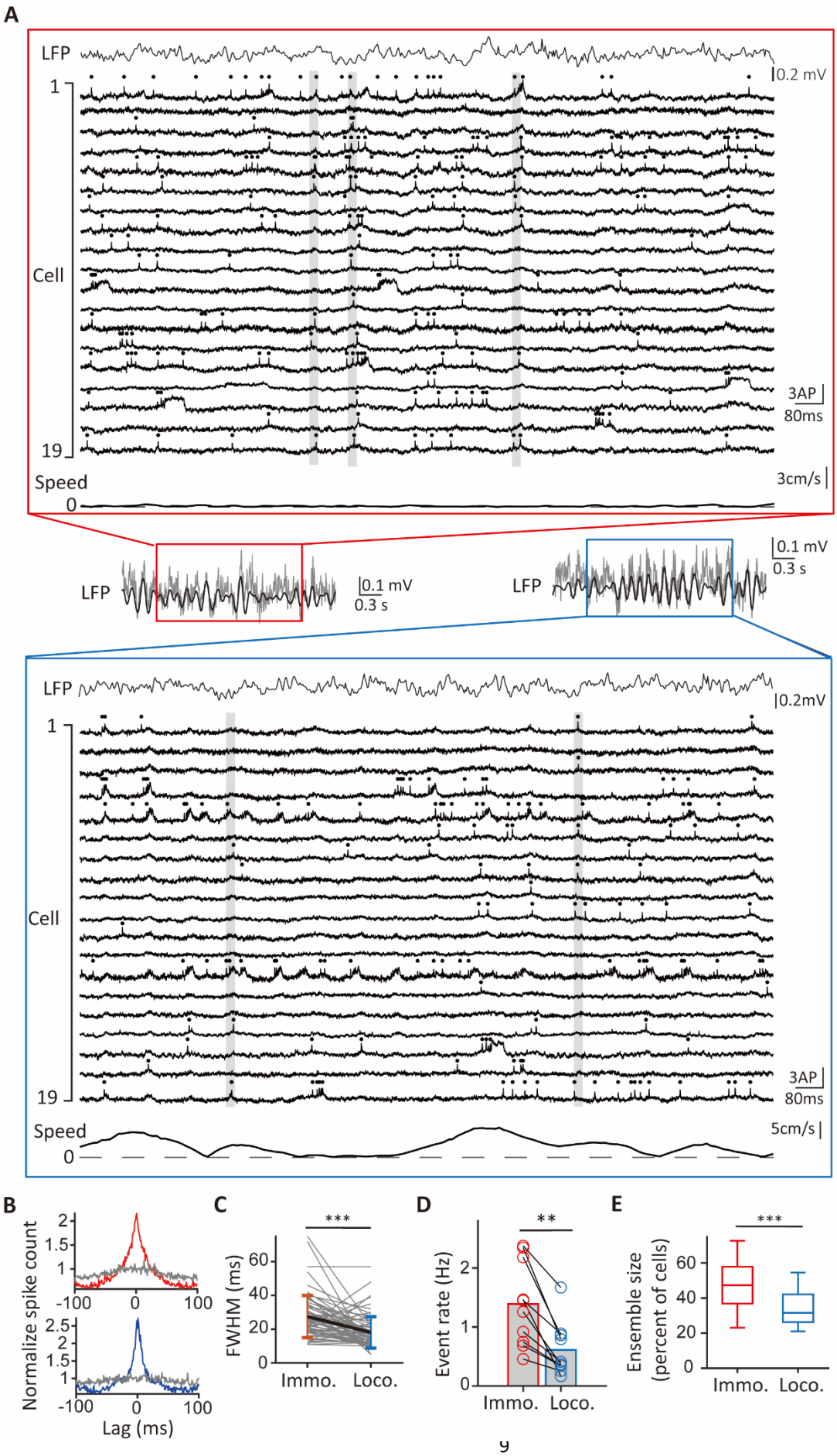
A
LFP
0.2 mV
1
Cell
19
3AP
80ms
Speed
0
3cm/s
LFP
0.1 mV
0.3 s
LFP
0.1 mV
0.3 s
LFP
0.2mV
1
Cell
19
3AP
80ms
Speed
0
5cm/s
B
Normalize spike count
Lag (ms)
C
FWHM (ms)
Immo.
Loco.
D
Event rate (Hz)
Immo.
Loco.
E
Ensemble size (percent of cells)
Immo.
Loco.

168

Figure 2 Comparison of synchronous ensembles between immobility and locomotion.

(A) Example traces of cells in a session with identified synchronous ensembles (gray rectangles) during periods of immobility (red rectangular frame) and locomotion (blue rectangular frame). Spikes are indicated by dots at the top of individual traces. Top: the simultaneously recorded LFP trace. Bottom: simultaneously recorded speed of the animal. Inset: the band-pass filtered LFP trace at the theta frequency range (black line) overlaid on the raw LFP trace (gray line).

(B) The grand average cross-correlograms (CCGs) during immobility (red) and locomotion (blue) averaged across all cells (n=71). The gray lines represent the mean grand average CCGs calculated from jittered data.

(C) Pairwise comparison of peak widths (FWHM) in the grand average CCGs between immobility (red) and locomotion (blue). Vertical bars represent means and standard deviations for both groups (FWHM: 27±12 ms for immobility, 18±9 ms for locomotion, mean±s.d., $p<0.001$, paired Student's *t*-test, n=71 cells). ***$p<0.001$

(D) Pairwise comparison of event rates of population synchrony during immobility and locomotion. Bar heights indicate group means (immobility: 1.4±0.7 Hz, locomotion: 0.6±0.5 Hz, mean±s.d., n=10 segments, $p=0.002$, Wilcoxon signed-rank test). **$p<0.01$

(E) Boxplot of ensemble sizes for synchronous ensembles occurring during immobility (red) and locomotion (blue) (median ensemble size: 47% for immobility, n=446 events, 32% for locomotion, n=313 events, $p<0.001$, Wilcoxon rank-sum test). ***$p<0.001$

Synchronous ensembles occur outside ripple episodes

CA1PCs exhibit synchronous activities when the hippocampal network emits ripple waves[8,14]. To test whether there is a co-occurrence of synchronous ensembles and ripples, we first detected ripples from LFP recordings. Ripples were detected in three of the five recording sessions, and all occurred during immobility (mean ripple rate: 0.04±0.02 Hz during immobility, 0 Hz during locomotion). In

the two recording sessions where we did not detect any ripples, we verified the recording quality of the LFP signal by running multiple tests after the recording sessions. Ripples were identified in the same animals during quality tests, indicating that the absence of ripples during novel immobility in the recording session was not due to the deterioration of LFP recordings (Fig. S3).

To visualize both ripples and synchronous ensembles, we plotted voltage traces of neurons alongside simultaneously recorded ripple oscillations. It was typical for synchronous ensembles to occur far away from ripple episodes (Fig. 3A). To delve into the relationship between neuronal activities and ripples, we aligned traces of ripple power with population synchrony and ripples. In a recording session where 64 synchronous ensembles and 12 ripples were detected during immobility, the LFP power at ripple frequency (120-240 Hz) exhibited no discernable peaks within any of the synchronous events (Fig. 3B, left upper and middle panels). Nevertheless, the same LFP power displayed substantial peaks during every ripple event (Fig. 3B, right upper and middle panels). A striking contrast between synchronous events and ripples was also evident when spiking probabilities during these events were examined. During population synchrony, the mean spiking probability averaged across all cells was high, while the spiking probability was almost zero during ripple events (Fig. 3B lower panel). In the three sessions where ripples were identified, we calculated the percentages of ripple events coinciding with synchronous ensembles and vice versa. Remarkably, there was no co-occurrence of ripples and synchronous ensembles (Fig. 3C). Furthermore, we quantified ripple-modulated spiking by calculating the ratio of the difference in mean firing rates during in-ripple and out-ripple periods to the sum of the mean firing rates during both periods. Indexes of most cells were negative, and a striking 85% of cells displayed ripple modulation indexes of -1, indicating complete suppression of their spiking activities during ripples (Fig. 3D). Taken together, during novel exploration, synchronous ensembles involved many neurons with millisecond-synchronized spikes and occurred outside the time frames of ripples.

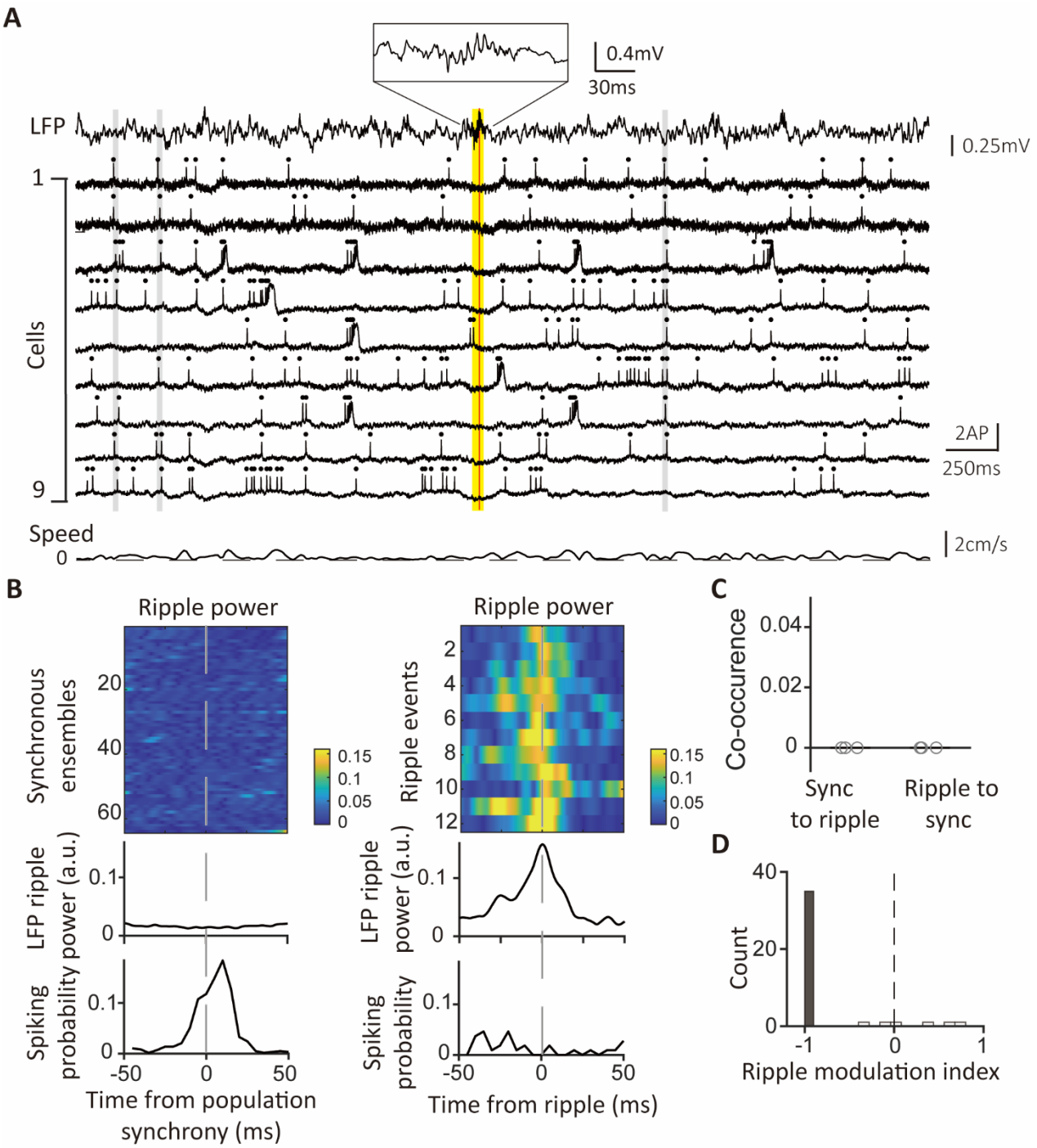

Figure 3 Synchronous ensembles occur outside ripple episodes.

(A) Example traces with ripples and synchronous ensembles. Top: simultaneously recorded LFP displaying an episode of ripple oscillation. A red vertical line indicates the timing of the peak ripple power in the LFP trace. A yellow rectangle marks the duration of the ripple episode. Inset at the top: a magnified view of the ripple oscillation. Middle: fluorescence traces of 9 CA1PCs. Gray rectangles mark the timings of the synchronous ensembles on all traces. Bottom: animals' speed recorded

simultaneously with voltage imaging.

(B) LFP ripple power and spiking probability aligned to synchrony ensembles and ripple events. Upper panel: color-coded LFP power at ripple frequency (120-240Hz) aligned to the timings of 64 synchronous ensembles (left) and 12 ripple events (right). Middle panel: Average LFP power of ripple frequency aligned to the timings of the synchronous ensembles (left) and the ripple events (right). Lower panel: Average spike counts of all cells aligned to the timings of the synchronous ensembles (left) and ripple events (right).

(C) Percentages of co-occurrences between population synchrony and ripples. The co-occurrences in the "sync to ripples" group represent the percentages of ripple episodes co-occurring with synchronous ensembles in the same episodes. The co-occurrences in the "ripples to sync" group indicate the percentages of synchronous ensembles co-occurring with ripple episodes. Each gray circle represents an individual session.

(D) Distribution of the ripple modulation indexes (n=41 cells). Gray bar: modulation indexes with significant p values (n=35 cells); white bars: modulation indexes without significance (n=6 cells).

Synchronous ensembles are associated with theta oscillations

To investigate the network dynamics associated with synchronous ensembles, we aligned LFP traces triggered by the timings of synchronous ensembles. The average LFP traces of a representative session showed prominent theta oscillations around the timings of both immobility and locomotion population synchrony (Fig. 4A). Spectral analysis of the mean synchrony-triggered LFP traces during immobility and locomotion revealed theta frequency components of 4-12 Hz, with a slightly higher peak frequency in locomotion LFP compared to immobility LFP (Fig. 4B). Furthermore, we computed LFP theta modulation and identified preferred phases of synchronous ensembles. In line with the previous result, synchronous ensembles displayed a high level of modulation by LFP theta oscillation (modulation strength: 0.61±0.05 during immobility and 0.74±0.04 during locomotion, n=5 sessions).

Although the preferred phases varied from session to session due to differences in recording sites along the proximal-distal axis of the hippocampus, the timings of individual ensembles were consistently locked to the preferred phase of each session (Fig. 4C). These results establish a strong link between synchronous ensembles and LFP theta oscillation.

Subthreshold membrane voltage (subVm) is one of the critical parameters supporting the generation of action potentials. To investigate the subthreshold signals underlying population synchrony, we aligned subVm traces with the timings of synchronous ensembles and observed that both immobility and locomotion synchrony rode on a subVm waveform oscillating at theta frequency (Fig. 4D). To elucidate further the relationship between subVm theta oscillation and spikes involved in population synchrony, we calculated the subVm theta modulation and preferred phases of spikes. Spikes participating in both immobility and locomotion synchrony were strongly coupled to the subVm theta oscillation of neurons, with the mean preferred phase being in the latter half of the rising phase closer to subVm theta peaks (Fig. 4E). Conversely, spikes not participating in synchronous ensembles had weaker modulation strength compared to spikes involved in synchrony (Fig. S4A and B). Furthermore, the membrane voltages triggered by these two categories of spikes showed a significant difference in the hyperpolarization phase of the theta oscillation. Synchronous spikes were situated within cycles of theta oscillations featuring more hyperpolarized troughs than spikes outside synchronous ensembles (Fig. S4C and D). Thus, compared to spikes not participating in synchronous ensembles, synchronous spikes showed a more robust modulation by theta oscillation of membrane voltage during immobility and locomotion in the context of novel exploration.

Notably, phase locking of spikes to their subVm theta oscillation and the synchronous spikes among many neurons suggest that subVms of different neurons would be correlated at the theta frequency. To explore the possibility, we divided the 180-second subVm traces into 1-second segments with

280 50% overlap and calculated the cross-correlation and magnitude-squared coherence function for
281 each pair of cell segments. Segments were sorted into the immobility or locomotion group based on
282 the animals' speed during each segment (kept below 1 cm/s for immobility and above 3 cm/s for
283 locomotion for more than 90% of the time). In total, we analyzed 511 cell pairs from 5 sessions.
284 Indeed, the cross-correlation of subVm between cell pairs revealed a high correlation at zero lag and
285 periodic modulation of the correlation at theta frequency (Fig. 4F). Furthermore, the subVm theta
286 coherences were increased in both groups (immobility: 0.50, locomotion: 0.40, median, n=511
287 pairs) and were negatively correlated with soma distances (immobility: -0.46, locomotion: -0.48,
288 n=511 pairs, Fig. 4G). Taken together, during novel exploration, CA1PCs generate synchronous
289 activity associated with theta oscillation and exhibit correlated and theta-coherent subVms.
290

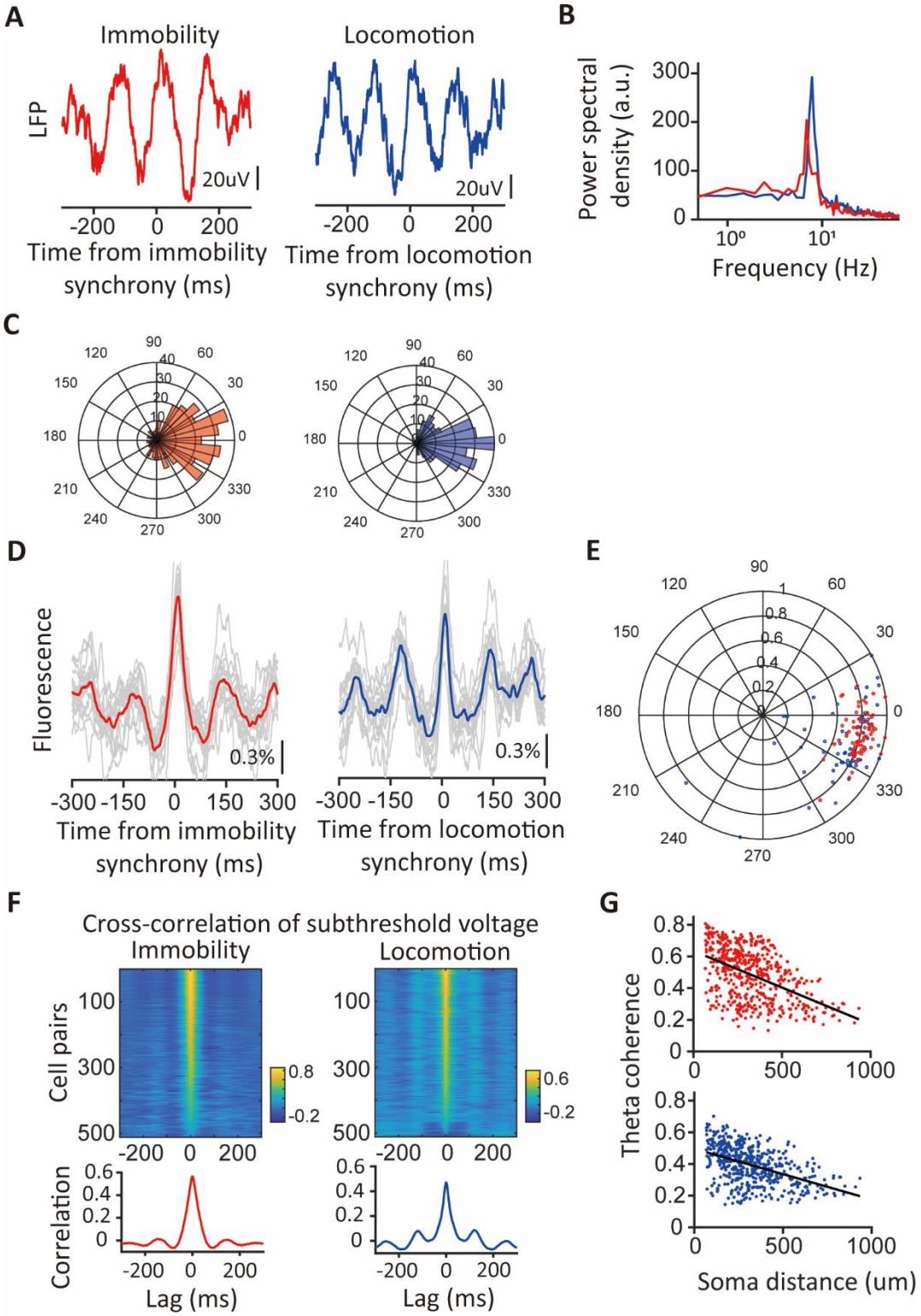

Figure 4 Theta oscillations in the LFP and subthreshold membrane potential were linked to population synchrony.

(A) LFP waveforms triggered by timings of synchronous ensembles. Red: triggered by timings of immobility synchrony; blue: triggered by timings of locomotion synchrony.

(B) Power spectral densities of the triggered LFP waveforms. Red: immobility; blue: locomotion.

(C) Distributions of the differences between LFP theta phases of individual synchronous ensembles and their preferred phases of the session. Note that most ensembles show minor differences within ±30 degrees. Red: immobility; blue: locomotion.

(D) Fluorescence traces triggered by timings of synchronous ensembles. Traces with spikes are excluded. Left panel: traces triggered by timings of immobility synchrony. Right panel: traces triggered by timings of locomotion synchrony. Thin gray lines: mean triggered fluorescence traces averaged across triggers for representative cells. Thick red and blue lines: mean triggered fluorescence traces averaged across cells.

(E) Polar plot illustrating theta modulation of spikes participating in the immobility synchrony (red dots) and of spikes participating in the locomotion synchrony (blue dots). The angle of the dots indicates the preferred phase, and the distance from the center of the circle represents the modulation strength. Each dot represents the averages from a neuron.

(F) Pairwise cross-correlation of the subthreshold membrane voltages (subVm). Top: color-coded cross-correlation of subVm between cell pairs during immobility and locomotion periods. Bottom: averaged cross-correlation over all cell pairs for immobility (red) and locomotion (blue) subVm. Both show a central peak at zero lag flanked by theta oscillation.

(G) Scatter plots of theta coherence against soma distances of immobility subVm (red) and locomotion subVm (blue) between cell pairs.

315 **Synchrony between place cells with distinct place tunings**

316 When animals explore a novel maze, spatially tuned spiking activity can form within a few
317 minutes[32,33]. However, how synchronous ensembles organize their spatially tuned activities during
318 novel exploration remains to be determined. Synchronous ensembles, generating spikes
319 coincidently in short intervals, might display correlated spiking at longer time windows that match
320 behavioral timescales of exploration, potentially leading to shared place responses. On the other
321 hand, CA1PCs are interconnected through inhibitory interneurons[34-36]. Modulation of activities in
322 inhibitory interneurons by some place cells may influence the activities of other place cells,
323 resulting in divergent spatial tunings[32,37,38].

324

325 To compare the spatial tunings of synchronous cell pairs, we first calculated the spatial tuning
326 curves of individual neurons by computing the mean firing rates in every spatial bin. On average,
327 40% of cells displayed selective spatial tunings of their spiking activities and were qualified as place
328 cells[39] (Fig. 5A). Among place cell pairs, some showed similar spatial tunings, while others did not
329 (Fig. 5B). For instance, in an illustrative session depicted in Fig. 5B, the seventh and eighth place
330 cells had highly similar spatial tunings with a correlation coefficient as high as 0.7. In contrast, the
331 fifth and tenth place cells exhibited vastly different spatial tunings with a correlation coefficient as
332 low as -0.5.

333

334 We further explored the relationship between the similarity of spatial tunings and synchronization
335 strength among pairs of place cells. We measured synchronization strength as the peak of the CCG
336 normalized by the averaged jittered spike count within the same bin as the CCG peak. We
337 segregated spikes based on these behavioral states to accommodate differences between
338 locomotion and immobility and calculated the corresponding CCG and synchronization strength.

339

340 During locomotion, we observed a robust negative correlation between synchronization strength

and the similarity of spatial tunings among cell pairs. In other words, cell pairs with more precisely co-active spikes during locomotion exhibited more distinct place-tuning profiles (Fig. 5C and D). This anti-correlation between synchronization strength and place tunings indicates coordination between place cells' temporal and spatial coding. On the other hand, synchronization strength during immobility showed little correlation with the similarity of spatial tunings among place cell pairs, suggesting that correlated activities at the millisecond timescale do not extend to slow, behavioral-relevant timescales (Fig. S5). Thus, place cells with distinct place fields are linked by synchronous activity during novel locomotion.

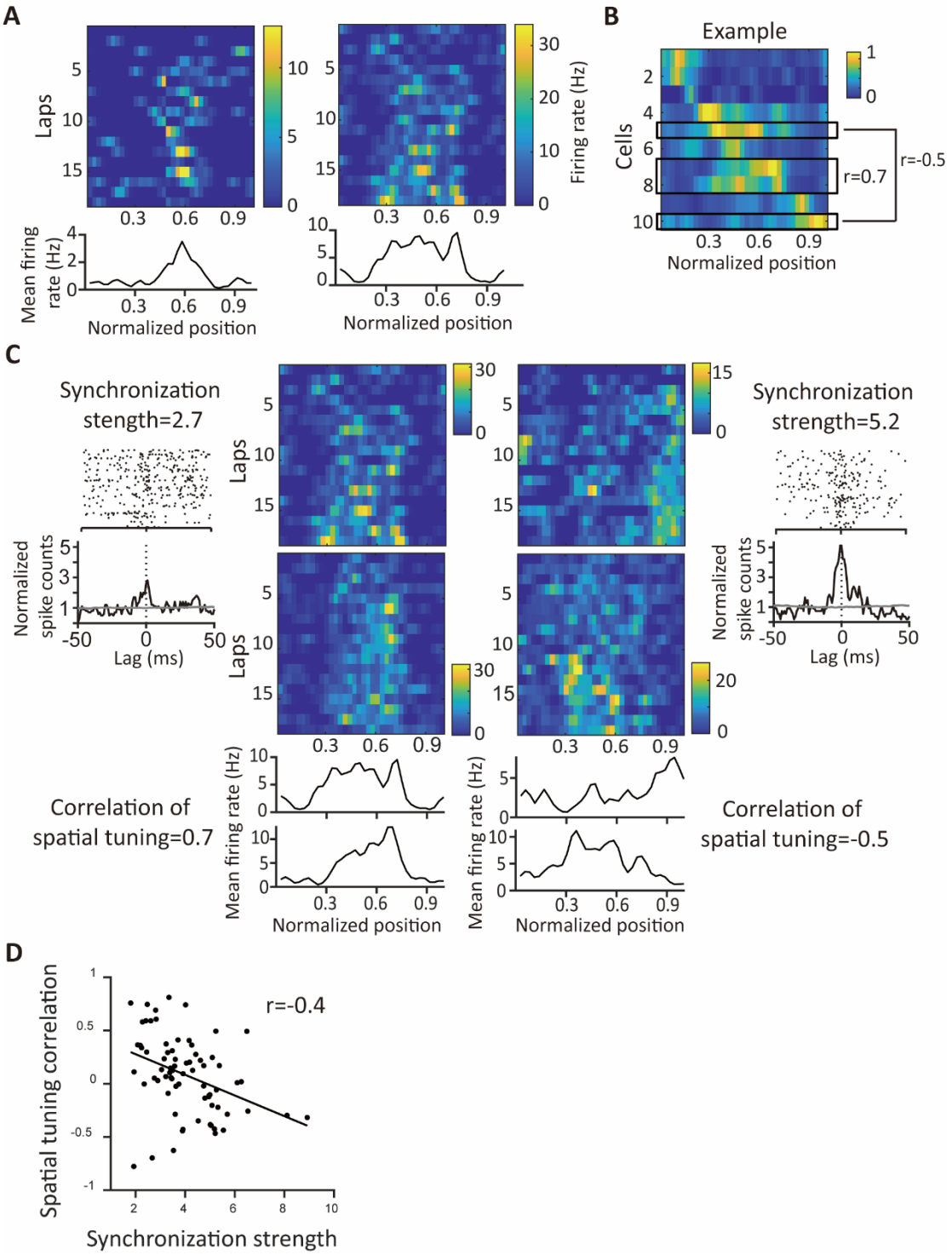

Figure 5 Negative correlation between spatial tuning similarity and synchronization strength during novel exploration.

(A) Spatially binned rate maps of place cells. High firing rates are indicated in yellow, and low firing rates are noted in blue. Bottom: the mean firing rates along spatial bins averaged across laps.

(B) Spatial tunings of 10 place cells from an example session. Cells are sorted based on the locations

356 of their peak firing rates.

357 **(C)** Two example pairs of neurons with cross correlograms during locomotion and spatially binned

358 firing rate maps.

359 **(D)** A scatter plot of correlation coefficients of spatial tunings against synchronization strengths for

360 place cell pairs. Each dot represents a pair of place cells. Synchronization strengths are negatively

361 correlated with similarities of spatial tunings (Spearman correlation coefficient=-0.4, $p<0.001$, n=73

362 pairs).

363

364

365 Discussion

366 Our findings reveal the presence of synchronous ensembles comprising a substantial number of

367 CA1PCs during both locomotion and immobility in a novel environment. These ensembles

368 concurrently engage neurons representing diverse aspects of the environment and are rarely

369 observed during ripple events. Instead, they closely align with LFP and intracellular theta

370 oscillations. Our data demonstrate theta-associated synchronous ensembles during spatial memory

371 acquisition, coordinating numerous CA1 place cells that transmit information about different

372 segments of the environment.

373

374 The correlation between observed population synchrony and theta oscillations is intriguing. Theta

375 oscillations are typically associated with the sequential activation of neurons over time, resulting in

376 reduced neuronal synchrony[22]. However, theta oscillations come in different types, each

377 characterized by distinct pharmacological properties and behavioral correlates[40-42]. For example,

378 type 1 theta, referred to as translational theta, occurs during voluntary movements and is sensitive

379 to N-methyl-D-aspartate receptor (NMDAR) blockers. On the other hand, type 2 theta, known as

380 attentional theta, is blocked by muscarinic receptor antagonists, emerging during states of arousal

381 or attention, such as entering a new environment[43-45].

During theta oscillations, cholinergic neurons in the medial septum excite downstream CA1PCs, leading to increased firing rates and membrane potentials[46-48]. Given the widespread influence of cholinergic inputs on numerous CA1PCs, theta-coupled cholinergic inputs may drive depolarization and firing across many CA1PCs. Additionally, they could enhance the likelihood of synchronicity. Furthermore, GABAergic neurons in the medial septum, activated during theta oscillations, could activate interneurons in the CA1 region[42,49,50]. These CA1 interneurons, in turn, have the capability to entrain the activities of pyramidal neurons at both sub- and suprathreshold levels, thereby promoting synchronization among pyramidal neurons[51,52]. In summary, cholinergic and GABAergic neuron activation during theta waves may contribute to the excitation of CA1PCs and the consequent increase in their synchronicity.

Theta oscillations have long been implicated in memory acquisition. Specifically, theta power correlates positively with learning performance[53-55]. Perturbing generation of theta waves leads to impairment in memory acquisition[56-60], while electrical stimulation restoring theta rhythms rescues learning performance[61,62]. Furthermore, increased spike-theta coherence correlates with better memory, and stimulations that boost theta phase-locking of spikes enhance memory[63-65]. Despite abundant evidence supporting a link between theta oscillations and memory, the precise network mechanism by which theta oscillations support memory acquisition remains unclear. Theta oscillations are hypothesized to link spatially distributed neurons into functional ensembles to support memory acquisition[13]. The identified synchronous ensembles support the hypothesis, providing a network substrate that links theta rhythms to the initial stage of memory acquisition.

Previous reports of CA1 synchronous ensembles occur predominantly during ripple oscillations[8,14,17]. However, we found only a few ripple events in the initial minutes of entering a new environment, even when animals are not moving. During these events, CA1PCs show decreased spiking activities, and they display synchronous firing outside ripple episodes (Fig.3).

409 Different from the ripple-associated synchronous ensembles described previously, the synchronous
410 ensembles we observed involve larger populations of neurons spiking synchronously in narrower
411 time intervals and are associated with theta oscillations. The absence of recorded ripple-associated
412 synchrony in our study may be attributed to elevated arousal with prominent theta oscillations even
413 during immobility, potentially suppressing ripples[66]. Additionally, the deep-layer CA1PCs imaged in
414 our study are known to show decreased activities during ripples, contributing to their lack of ripple-
415 associated synchrony[67]. The CA1 network may generate multiple types of population synchrony,
416 with ripple-associated synchrony facilitating memory consolidation, while the newly identified theta
417 population synchrony supports the initial stage of memory acquisition.
418
419 Although CA1PCs are known to exhibit weaker recurrent connectivity than that of CA3 pyramidal
420 neurons, CA1PCs did communicate through monosynaptic connections[68]. These connections can be
421 dynamically adjusted by the spike-timing-dependent plasticity mechanism[69-71], and therefore could
422 be affected by the transient population synchrony. In addition, CA1PCs are known to communicate
423 through inhibitory interneurons. Multiple pyramidal neurons converge onto a single interneuron,
424 and individual connections are often weak and unreliable[35,72,73]. This connectivity scheme requires
425 multiple pyramidal neurons spiking synchronously within the time window of synaptic integration to
426 effectively activate postsynaptic neurons[35]. Furthermore, population synchrony among CA1PCs may
427 propagate to downstream areas, synchronizing neurons outside the hippocampus. With their large
428 ensemble sizes, these synchronous ensembles may synergistically convey relevant information or
429 reorganize the connectivity of the neuronal networks.
430
431 Prior studies in sensory systems have commonly revealed that neurons with synchronous activities
432 typically share similar sensory responses[74,75]. However, the synchronous ensembles we have
433 identified often encompass neurons with distinct preferences for place fields. Pairwise synchrony
434 demonstrates a negative correlation with place field overlap (Fig. 5). These findings indicate that

synchrony does not necessarily imply similar tunings between neurons. Furthermore, these synchronous ensembles involve place cells encoding different spatial information. Recognizing the crucial role of neuronal synchrony in binding distributed neurons in the brain[3,5], population synchrony may serve as a mechanism to integrate diverse features of the same environment into a cohesive mental map.

Methods

Animal

Time-pregnant wild-type C57BL/6J female mice underwent in utero virus injection of CamkII-cre virus (105558-AAV1, Addgene) into the left side of the lateral ventricles. The resulting offspring were raised in a breeding room under controlled temperature and humidity conditions and a 12-hour light/dark cycle (lights on from 7:00 to 19:00). The mice used in the experiments were between 12 and 18 weeks old at the time of the recordings. All surgical procedures, behavioral training, and recording protocols were approved by the NYCU Institutional Animal Care and Use Committee.

In-utero virus injection

Time-pregnant mice on an embryonic day 14.5 were anesthetized with isoflurane (induction:4-5%; maintenance:1-3%) before surgery. The animals were placed on a heating pad in a supine position to maintain body temperature. Aseptic procedures were implemented to maintain sterile conditions during the surgery. Uterine horns were exposed one at a time using spoons and fingers. Warm and sterile phosphate-buffered saline (PBS) was used to rinse the uterus to prevent it from drying out. Micropipettes loaded with CamkII-cre virus solution were used to inject 0.2 uL of virus suspension into the left side of the lateral ventricle of each embryo. The uterine horn was then gently returned to the abdominal cavity. The exact process was repeated to the other uterine horn. After the surgery, ketorolac (6mg/kg) and cefazolin (1g/kg) were administered for two days to minimize pain and inflammation.

Cranial window and cannula implantation

The offspring of the mice that had undergone in-utero injection were subjected to chronic hippocampal window surgery when they were between 2 and 4 months old. The animals were

467 initially anesthetized using isoflurane (induction:4-5%; maintenance:1-3%). Topical anesthesia was
468 applied by administering 0.5% lidocaine to the wound margins. After achieving deep anesthesia, an
469 incision was made in the skin, and a circular section of the skull was removed, centered 2 mm
470 caudal and 1.8 mm left to the bregma. Using 30-gauge needles and forceps, the dura was removed
471 from the exposed area, and cortical tissue within the craniotomy was aspirated. A fine injection
472 pipette (tip diameter 10-60 um) was used to inject AAV2/1-CAG-flex-Voltron2-ST ($2.7x10^{12}$ GC/ml, a
473 courtesy gift from Dr. Eric Schreiter and the GENIE team at HHMI Janelia Research Campus) into the
474 exposed regions at a depth of 200 μm (up to six injection sites and 100-200 nL of viral
475 suspension). An optical chamber was constructed by placing a cannula with a cover slip attached at
476 the bottom over the craniotomy and sealing it with dental acrylic or C&B Metabond (Sun Medical).
477 A custom-built titanium frame was then cemented to the animal's head using dental acrylic or C&B
478 Metabond. Mice received ketorolac (6mg/kg) and cefazolin (1g/kg) for two days following surgery to
479 minimize pain and inflammation.
480
481 **Behavioral training**
482 After at least two weeks of recovery from the window surgery, the mice underwent behavioral
483 training to ensure they were calm and attentive in the test environment. The initial training phase
484 involved acclimating the mice to head fixation and treadmill running, which took place over 3-5 days
485 in a separate room distinct from the recording setup. Following this training, the imaging
486 experiments were conducted. On the day designated for imaging, the mice were introduced to the
487 recording room for the first time just before the imaging session. During the imaging experiments,
488 the mice were securely held in a head-fixed position beneath the microscope and on an air-lifted
489 plastic track that rested on an air table (AirLift, Neurotar; Fig. 1Aa). The track was adorned with
490 various shapes of signs to help the mice navigate the track. Subdued blue lighting was provided to
491 illuminate the track. Before the initiation of imaging, the mice were confined in a corner of the track
492 using gates. Subsequently, the gates were opened upon the start of imaging, allowing the mice to

493 explore the new environment during their initial laps (Fig. 1Ab). The Mobile HomeCage tracking
494 system (Neurotar) was used to track the mice's position and speed. During the acquisition of image
495 frames, TTL pulses were sent by the high-speed camera to the Mobile HomeCage tracking system to
496 facilitate data alignment.
497
498 **Voltage imaging**
499 Imaging was performed after treadmill training. JF_{552}-HaloTag ligand[76] (a courtesy gift from Dr. Luke
500 Lavis) was first dissolved in DMSO (Sigma) and then diluted in Pluronic™ F-127 (P3000MP,
501 Invitrogen) and PBS to achieve a final concentration of 0.83 mM of JF_{552}-HaloTag ligand. The
502 solution was then injected intravenously through the retro-orbital sinus. Imaging sessions were
503 initiated 3-5 hours after the injection of the JF_{552}-HaloTag ligand. Fluorescence sensors were excited
504 using a 532-nm laser (Opus 532, Laser Quantum) with an excitation filter (FF02-520-28, Semrock),
505 and the emitted light was separated from the excitation light using a dichroic mirror (540lpxr
506 Chroma) and passed through an emission filter (FF01-596183 Semrock). A 16X, 0.8 NA objective
507 (Nikon) was used to collect the emission light which was then imaged on a CMOS camera (DaVinci-
508 1K, RedShirt) with a 50-mm camera lens (Nikkor 50mm f1.2, Nikon) as the tube lens. Images were
509 acquired using Turbo-SM64 (Sci-Measure) at 2kHz with a resolution of 190 x 160 pixels,
510 corresponding to a field of view of 1.4 x 1.2 mm. The number of frames in an image session was set
511 at 360,000, corresponding to a duration of 180 seconds per session. Imaging depths ranged
512 between 70 and 170 μm from the window surface, where the CA1 pyramidal neurons were
513 located. Time-lapse images were collected, and image stacks of the same field of view along the z-
514 axis were acquired. The image stacks consisted of 100 plans separated by two μm, covering the
515 depth from the window surface to 200 um from the surface.
516
517 **LFP recording**
518 The LFP signal from the contralateral CA1 region of the hippocampus was simultaneously recorded

519 during voltage imaging. To implant the LFP electrode, a small craniotomy was performed at the
520 dorsal CA1 coordinate (2mm caudal and 1.8 mm right to the bregma). A tungsten electrode
521 (#100211, 38 μm in diameter, polyimide insulated, California Fine Wire) was inserted into the
522 dorsal CA1 region, and the wire and pins were cemented in place with dental acrylic. The electrical
523 signal was amplified and filtered (1-1kHz) using a DAM80 amplifier (Word Precision Instruments).
524 The amplified signal was acquired by an I/O device (National Instruments USB-6341) and recorded
525 using WaveSurfer (Adam Taylor, HHMI Janelia Research Campus) at 10 kHz during implantation and
526 TurboSM64 (RedShirt) at 8 kHz during imaging.
527
528 **Voltage imaging preprocessing and spike detection**
529 Fluorescence intensities were corrected for brain movement using rigid registration. Regions of
530 interest (ROIs) were manually selected by grouping pixels that cover individual somata. The
531 fluorescence intensities of individual neurons were calculated by averaging the fluorescence
532 intensities of pixels from the same ROIs. Bleaching was corrected by calculating the baseline
533 fluorescence (F_0) at each time point as an average of the fluorescence intensities within $\pm$0.5 s
534 around the time point. The dF/F was calculated as the F_0 minus the fluorescence intensity of the
535 same time point divided by F_0. Positive fluorescence transients were detected to identify spikes
536 from the high-passed dF/F traces created by subtracting the dF/F traces from the median-filtered
537 version with a 5-ms window. To simulate the noise of recordings, high-passed dF/F traces were
538 inverted, and the amplitudes of the transients detected from the inverted traces were used to
539 construct a noise distribution of the spike amplitudes. A threshold was set by comparing the
540 amplitudes of the detected transients with the noise distribution of the spike amplitudes to
541 minimize the sum of type I and type II errors. Spikes were first detected when transients were larger
542 than the threshold. Then, spike amplitudes smaller than half of the top 5% spike amplitudes were
543 excluded. The signal-to-noise ratio (SNR) was calculated for each neuron as a ratio of the averaged
544 spike amplitudes over the standard deviation of the high-passed dF/F traces, excluding points 2 ms

before and 4 ms after each detected spike to estimate the quality of the recordings. The crosstalk between ROIs was routinely checked by examining the refractory periods of neurons in auto-correlograms. Only neurons meeting the following criteria were included: (1) SNR larger than 5, (2) full width at half maximum of the spike waveform longer than 0.8 ms, (3) mean spike rates higher than 0.1 Hz, (4) distances between soma pairs at least 70 μm. Sessions with at least nine neurons meeting the selection criteria were used for further analysis. Based on these criteria, we included five sessions containing 9, 11, 13, 19, and 19 neurons.

Behavioral states of locomotion and immobility

The periods of locomotion were defined as instances when the animals' speed exceeded 3 cm/s, while periods of immobility were determined as instances when the animals' speed fell below 1 cm/s.

Mean firing rates during locomotion and immobility

To calculate the mean firing rates during locomotion, we counted the number of spikes during locomotion periods and divided this number by the total duration of locomotion. Similarly, for mean firing rates during immobility, we calculated the number of spikes that occurred during immobility periods and divided this number by the total duration of immobility.

Correlation between instantaneous firing rate and animal speed

To estimate the instantaneous firing rates of individual neurons over time, we convolved their spike trains with a Gaussian window of 250 ms. Subsequently, we calculated the Pearson correlation coefficient between these instantaneous firing rates and the animal's speed for each neuron.

Grand average cross-correlogram (CCG)

Grand average CCGs were generated by constructing histograms of relative spike timings between

spikes of a reference cell and spikes of all other neurons in the same session as the target cell population. Histograms were binned using 1-ms time bins. Spike counts were normalized by the number of reference spikes times the number of all other neurons. An equal number of cells from different sessions were randomly selected to form the shuffled target cell population to assess the statistical significance of the CCG peaks. Subsequently, grand average CCGs were computed using shuffled spike trains for comparison. Grand average CCGs were calculated using all spikes in the 180-s recording periods, subsets of spikes during immobility periods (immobility grand average CCGs), and subsets of spikes during locomotion periods (locomotion grand average CCGs).

Detection of the population synchrony

To assess population synchrony, we counted the number of spikes from all neurons within a sliding window of 25 ms. To test the significance of the synchrony, we generated surrogate data by jittering spike timings within a ±75-ms window. By comparing the spike counts between the original and jittered populations, we determined population synchrony when the spike count was higher than the mean plus four standard deviations of the jittered spike counts. To estimate synchronous event rates, we divided the entire 180-s recordings into halves and calculated the event rate in each of the 90-s segments. Additionally, we quantified the ensemble sizes by counting the percentage of participating neurons in each synchronous event.

Pairwise cross-correlogram (CCG) of neuronal pairs

To compute the CCG, we first determined the time difference between spikes in the target and reference neurons and then binned these values into 1-ms time bins. CCGs were only computed for pairs with more than 100 counts within the CCG window of ±500 ms to ensure reliable correlation. We defined the peak of the CCG as the local maxima within ±30 ms of lag. To assess the significance of cross-correlations, we generated surrogate data by jittering the spike times of the target neuron

596 within a ±75 ms window. We computed the CCG peak for a thousand iterations and calculated p-
597 values by comparing the percentile of the peak in the null distribution of the jittered peak values.
598 The synchronization strength was estimated as the ratio between the original CCG peak and the
599 mean spike count of the same bin as the original CCG peak averaged across the jittered histograms.
600 For display purposes, the CCGs were smoothed using a 5-point moving average. CCGs were
601 calculated using all spikes in the 180-s recording periods, subsets of spikes during immobility
602 periods (immobility pairwise CCGs), and subsets of spikes during locomotion periods (locomotion
603 pairwise CCGs).
604
605 **LFP ripple analysis**
606 To detect ripples, we performed band-pass filtering of the LFP signal between 120 and 240 Hz,
607 followed by computing the envelope using the absolute values of the Hilbert transform, which was
608 then low-pass filtered at 20 Hz. The start and end times of ripples were identified by setting the
609 upper and lower thresholds at the mean plus 7 and 3.5 times the standard deviation of the
610 envelope, respectively. For a ripple event to be included, three conditions had to be met: (1) values
611 within the event were higher than the lower threshold, (2) at least one value exceeded the upper
612 threshold, and (3) the minimum duration of the event was 30 ms. The start and end times of a
613 ripple event were defined as the positive and negative crossings of the lower threshold,
614 respectively. We defined in-ripple periods as the time between the start and end of detected LFP
615 ripple events, while out-ripple periods were periods outside the in-ripple periods. The envelope
616 peak values of the detected ripple events were used as the time of ripple occurrence. These timings
617 were utilized as trigger timings to calculate averages triggered by ripples. Two co-occurrences were
618 quantified: the percentages of LFP ripple oscillations that occurred with synchronous ensembles
619 and the percentages of synchronous ensembles that occurred with LFP ripple oscillations.
620
621 **Ripple modulation index**

We utilized the ripple modulation index to assess changes in firing rates during ripples compared to periods outside ripples. This index was computed as the ratio of the difference in mean firing rates during in- and out-ripple periods to the sum of the mean firing rates during both periods. Specifically, we first calculated the mean firing rate during in-ripple periods and the mean firing rate during out-ripple periods. Next, we subtracted the mean firing rate during out-ripple periods from the mean firing rate during in-ripple periods and divided the result by the sum of the mean firing rates during both periods. The resulting ripple modulation index indicates the magnitude and direction of the firing rate modulation during ripple compared to periods outside ripples.

LFP traces triggered by population synchrony and analysis

The midpoints of the synchronous event intervals were utilized as triggers to align LFP traces. These traces were aligned within a ± 1-second window around the trigger time points. To calculate the spectral density functions of the aligned LFP traces, we performed a 16,384-point fast Fourier transform of the 2-second LFP traces. The power spectra were then estimated as the squared absolute values of the Fourier coefficients. Ripple power was calculated as the sum of the power distributed between 120 and 240 Hz. To calculate theta modulation strength and preferred angles of the synchronous ensembles, LFP was first filtered within the theta frequency range. Then, the phase $\varphi(t)$ and the instantaneous amplitude $A(t)$ of the filtered LFP were computed using the Hilbert transform. A vector $V_k = A(t_k)e^{i\varphi(t_k)}$ was assigned to each synchronous ensemble that occurred at time t_k. The modulation strength and the preferred phase angle were determined as the absolute value and the phase angle of the summed vector over all ensembles, respectively. Modulation strengths were normalized by the total length of all vectors.

Subthreshold membrane voltage (subVm)

To compute the subVm of individual neurons, we began by determining the difference between the raw dF/F signal and the high-pass version of dF/F. Next, we calculated the spike threshold for each

cell by identifying the voltage value corresponding to the peak of the first derivative of the spike waveforms. Any fluorescence values in the slow dF/F time courses that surpassed the spike thresholds were linearly interpolated.

SubVm traces triggered by population synchrony

The midpoint of the time intervals, during which synchronous ensembles were detected, served as the reference points for aligning fluorescence traces within a $\pm$300 ms window around those reference points. To eliminate any interference from membrane potential fluctuations associated with spikes, we excluded aligned traces in cases where any spike occurred within the time intervals of the aligned traces.

SubVm theta modulation and phase preference of spikes occurred inside and outside the population synchrony events

The subVm was initially filtered within the theta frequency range. Subsequently, the phase $\varphi(t)$ and the instantaneous amplitude $A(t)$ of the filtered subVm were computed using the Hilbert transform. Spikes were categorized into four groups: those occurring during or outside immobility synchronous events and those occurring during or outside locomotion synchronous events. Within each category, a vector $V_k = A(t_k)e^{i\varphi(t_k)}$ was assigned to each spike that occurred at time t_k. The modulation strength and the preferred phase angle were determined as the absolute value and the phase angle of the summed vector over all spikes, respectively. Modulation strengths were normalized by the total length of all vectors to facilitate comparison between neurons.

Spike-triggered fluorescence traces

We extracted segments of fluorescence traces using a $\pm$300 ms time window centered on the spike timings. To examine variations in fluorescence waveforms triggered by spikes within and outside synchronous events, we categorized the fluorescence traces based on whether the spikes occurred

674 within or outside these events. Subsequently, we performed pairwise comparisons of the
675 fluorescence values from the same neuron, concentrating on spikes occurring during corresponding
676 behavioral states. Neurons with fewer than four triggering events in any of these categories were
677 omitted from the analysis.
678
679 **Cross-correlation and coherence analysis to the subVm traces**
680 To calculate cross-correlation and theta coherence of subVm between pairs of neurons during
681 locomotion and immobility, we initially divided the 180-second subVm traces into 1-second
682 segments with a 50% overlap. These segments were then categorized into the locomotion group if
683 the animal's speed remained above three cm/s for more than 90% of the time within that segment.
684 Similarly, segments were sorted into the immobility group if the animal's speed remained below
685 one cm/s for more than 90% of the time within that segment. Subsequently, we computed the
686 cross-correlation and magnitude-squared coherence function of frequency for pairs of co-occurred
687 segments belonging to a specific cell pair. Mean cross-correlations of individual cell pairs were
688 averaged across segments that occurred in the same behavioral states (i.e., locomotion or
689 immobility states). To estimate theta coherence, we averaged the values of the coherence function
690 within the theta frequency range (4-12 Hz). Theta coherences from the same cell pair during the
691 same behavioral state were pooled together, and the average was used as an estimate for the theta
692 coherence of that cell pair during a particular behavioral state. Finally, Spearman correlation
693 coefficients were calculated between the mean theta coherences of cell pairs and their soma
694 distances.
695
696 **Spatial analysis**
697 We partitioned a 90-cm-long track into 36 spatial bins to analyze spatial tuning properties. For each
698 cell, the spatial tuning curve was computed by determining the mean firing rate, defined as the
699 number of spikes within the bin when the animal's speed exceeded three cm/s, divided by the total

700 dwell times using the same speed threshold. The peak firing rates were identified as the maximal
701 rate on the spatial tuning curve. Spatial selectivity was calculated as one minus the circular variance
702 of the spatial tuning curve. Neurons were classified as place cells when their spatial selectivity
703 exceeded 0.25, and peak firing rates exceeded 1 Hz. To assess the similarity of spatial tuning
704 between pairs of neurons, Spearman correlation coefficients were calculated for the spatial tuning
705 curves. To explore the relationship between levels of synchronization and spatial tuning similarity
706 among pairs of place cells, Spearman correlation coefficients were computed between
707 synchronization strengths of cell pairs and correlation coefficients of their spatial tuning curves.
708
709 **Data analysis and statistics**
710 Data analysis was performed using MATLAB (Mathworks, R2019b), and results were presented as
711 standard error of the mean unless otherwise specified. Boxplots were used to depict the median,
712 first quartile, and third quartile, with the middle line, the upper edge, and the lower edge of the
713 box, respectively. The whiskers of the boxplots represented the 5th and 95th percentiles of the
714 distribution.
715

1 Takeuchi, T., Duszkiewicz, A. J. & Morris, R. G. The synaptic plasticity and memory hypothesis: encoding, storage and persistence. *Philos Trans R Soc Lond B Biol Sci* **369**, 20130288 (2014). https://doi.org:10.1098/rstb.2013.0288

2 Moser, M. B., Rowland, D. C. & Moser, E. I. Place cells, grid cells, and memory. *Cold Spring Harb Perspect Biol* **7**, a021808 (2015). https://doi.org:10.1101/cshperspect.a021808

3 Axmacher, N., Mormann, F., Fernandez, G., Elger, C. E. & Fell, J. Memory formation by neuronal synchronization. *Brain Res Rev* **52**, 170-182 (2006). https://doi.org:10.1016/j.brainresrev.2006.01.007

4 Paulsen, O. & Sejnowski, T. J. Natural patterns of activity and long-term synaptic plasticity. *Curr Opin Neurobiol* **10**, 172-179 (2000). https://doi.org:10.1016/s0959-4388(00)00076-3

5 Wang, X. J. Neurophysiological and computational principles of cortical rhythms in cognition. *Physiol Rev* **90**, 1195-1268 (2010). https://doi.org:10.1152/physrev.00035.2008

6 Harris, K. D., Csicsvari, J., Hirase, H., Dragoi, G. & Buzsaki, G. Organization of cell assemblies in the hippocampus. *Nature* **424**, 552-556 (2003). https://doi.org:10.1038/nature01834

7 Squire, L. R. & Wixted, J. T. The cognitive neuroscience of human memory since H.M. *Annu Rev Neurosci* **34**, 259-288 (2011). https://doi.org:10.1146/annurev-neuro-061010-113720

8 Buzsaki, G. Hippocampal sharp wave-ripple: A cognitive biomarker for episodic memory and planning. *Hippocampus* **25**, 1073-1188 (2015). https://doi.org:10.1002/hipo.22488

9 Nadasdy, Z., Hirase, H., Czurko, A., Csicsvari, J. & Buzsaki, G. Replay and time compression of recurring spike sequences in the hippocampus. *J Neurosci* **19**, 9497-9507 (1999). https://doi.org:10.1523/JNEUROSCI.19-21-09497.1999

10 Cheng, S. & Frank, L. M. New experiences enhance coordinated neural activity in the hippocampus. *Neuron* **57**, 303-313 (2008). https://doi.org:10.1016/j.neuron.2007.11.035

11 Dragoi, G. & Tonegawa, S. Preplay of future place cell sequences by hippocampal cellular assemblies. *Nature* **469**, 397-401 (2011). https://doi.org:10.1038/nature09633

12 Liu, C., Todorova, R., Tang, W., Oliva, A. & Fernandez-Ruiz, A. Associative and predictive hippocampal codes support memory-guided behaviors. *Science* **382**, eadi8237 (2023). https://doi.org:10.1126/science.adi8237

13 Colgin, L. L. Rhythms of the hippocampal network. *Nat Rev Neurosci* **17**, 239-249 (2016). https://doi.org:10.1038/nrn.2016.21

14 Buzsaki, G. & Silva, F. L. High frequency oscillations in the intact brain. *Prog Neurobiol* **98**, 241-249 (2012). https://doi.org:10.1016/j.pneurobio.2012.02.004

15 Csicsvari, J., Hirase, H., Czurko, A. & Buzsaki, G. Reliability and state dependence of pyramidal cell-interneuron synapses in the hippocampus: an ensemble approach in the behaving rat. *Neuron* **21**, 179-189 (1998). https://doi.org:10.1016/s0896-6273(00)80525-5

16 Gillespie, A. K. *et al.* Hippocampal replay reflects specific past experiences rather than a plan for subsequent choice. *Neuron* **109**, 3149-3163 e3146 (2021). https://doi.org:10.1016/j.neuron.2021.07.029

17 Yagi, S., Igata, H., Ikegaya, Y. & Sasaki, T. Awake hippocampal synchronous events are incorporated into offline neuronal reactivation. *Cell Rep* **42**, 112871 (2023). https://doi.org:10.1016/j.celrep.2023.112871

18 El-Gaby, M. *et al.* An emergent neural coactivity code for dynamic memory. *Nat Neurosci* **24**, 694-704 (2021). https://doi.org:10.1038/s41593-021-00820-w

19 Skaggs, W. E., McNaughton, B. L., Wilson, M. A. & Barnes, C. A. Theta phase precession in hippocampal neuronal populations and the compression of temporal sequences. *Hippocampus* **6**, 149-172 (1996). https://doi.org:10.1002/(SICI)1098-1063(1996)6:2<149::AID-HIPO6>3.0.CO;2-K

20 Dragoi, G. & Buzsaki, G. Temporal encoding of place sequences by hippocampal cell assemblies. *Neuron* **50**, 145-157 (2006). https://doi.org:10.1016/j.neuron.2006.02.023

21 Foster, D. J. & Wilson, M. A. Hippocampal theta sequences. *Hippocampus* **17**, 1093-1099 (2007). https://doi.org:10.1002/hipo.20345

22 Mizuseki, K. & Buzsaki, G. Theta oscillations decrease spike synchrony in the hippocampus and entorhinal cortex. *Philos Trans R Soc Lond B Biol Sci* **369**, 20120530 (2014). https://doi.org:10.1098/rstb.2012.0530

23 O'Keefe, J. & Recce, M. L. Phase relationship between hippocampal place units and the EEG theta rhythm. *Hippocampus* **3**, 317-330 (1993). https://doi.org:10.1002/hipo.450030307

24 Lee, A. K. & Brecht, M. Elucidating Neuronal Mechanisms Using Intracellular Recordings during Behavior. *Trends Neurosci* **41**, 385-403 (2018). https://doi.org:10.1016/j.tins.2018.03.014

25 Petersen, C. C. H. Whole-Cell Recording of Neuronal Membrane Potential during Behavior. *Neuron* **95**, 1266-1281 (2017). https://doi.org:10.1016/j.neuron.2017.06.049

26 Giocomo, L. M., Zilli, E. A., Fransen, E. & Hasselmo, M. E. Temporal frequency of subthreshold oscillations scales with entorhinal grid cell field spacing. *Science* **315**, 1719-1722 (2007). https://doi.org:10.1126/science.1139207

27 Lampl, I., Reichova, I. & Ferster, D. Synchronous membrane potential fluctuations in neurons of the cat visual cortex. *Neuron* **22**, 361-374 (1999). https://doi.org:10.1016/s0896-6273(00)81096-x

28 Poulet, J. F. & Petersen, C. C. Internal brain state regulates membrane potential synchrony in barrel cortex of behaving mice. *Nature* **454**, 881-885 (2008). https://doi.org:10.1038/nature07150

29 Abdelfattah, A. S. *et al.* Sensitivity optimization of a rhodopsin-based fluorescent voltage indicator. *Neuron* (2023). https://doi.org:10.1016/j.neuron.2023.03.009

30 Adam, Y. *et al.* Voltage imaging and optogenetics reveal behaviour-dependent changes in hippocampal dynamics. *Nature* **569**, 413-417 (2019). https://doi.org:10.1038/s41586-019-1166-7

31 Klausberger, T. *et al.* Brain-state- and cell-type-specific firing of hippocampal interneurons in vivo. *Nature* **421**, 844-848 (2003). https://doi.org:10.1038/nature01374

32 Rolotti, S. V. *et al.* Local feedback inhibition tightly controls rapid formation of hippocampal place fields. *Neuron* **110**, 783-794 e786 (2022). https://doi.org:10.1016/j.neuron.2021.12.003

33 Sheffield, M. E. J., Adoff, M. D. & Dombeck, D. A. Increased Prevalence of Calcium Transients across the Dendritic Arbor during Place Field Formation. *Neuron* **96**, 490-504 e495 (2017). https://doi.org:10.1016/j.neuron.2017.09.029

34 Takacs, V. T., Klausberger, T., Somogyi, P., Freund, T. F. & Gulyas, A. I. Extrinsic and local glutamatergic inputs of the rat hippocampal CA1 area differentially innervate pyramidal cells and interneurons. *Hippocampus* **22**, 1379-1391 (2012). https://doi.org:10.1002/hipo.20974

35 English, D. F. *et al.* Pyramidal Cell-Interneuron Circuit Architecture and Dynamics in Hippocampal Networks. *Neuron* **96**, 505-520 e507 (2017). https://doi.org:10.1016/j.neuron.2017.09.033

36 Maccaferri, G., Roberts, J. D., Szucs, P., Cottingham, C. A. & Somogyi, P. Cell surface domain specific postsynaptic currents evoked by identified GABAergic neurones in rat hippocampus in vitro. *J Physiol* **524 Pt 1**, 91-116 (2000). https://doi.org:10.1111/j.1469-7793.2000.t01-3-00091.x

37 Geiller, T. *et al.* Local circuit amplification of spatial selectivity in the hippocampus. *Nature* **601**, 105-109 (2022). https://doi.org:10.1038/s41586-021-04169-9

38 Trouche, S. *et al.* Recoding a cocaine-place memory engram to a neutral engram in the hippocampus. *Nat Neurosci* **19**, 564-567 (2016). https://doi.org:10.1038/nn.4250

39 Go, M. A. *et al.* Place Cells in Head-Fixed Mice Navigating a Floating Real-World Environment. *Front Cell Neurosci* **15**, 618658 (2021). https://doi.org:10.3389/fncel.2021.618658

40 Kramis, R., Vanderwolf, C. H. & Bland, B. H. Two types of hippocampal rhythmical slow activity in both the rabbit and the rat: relations to behavior and effects of atropine, diethyl ether, urethane, and pentobarbital. *Exp Neurol* **49**, 58-85 (1975). https://doi.org:10.1016/0014-4886(75)90195-8

41 Bland, B. H. The physiology and pharmacology of hippocampal formation theta rhythms. *Prog Neurobiol* **26**, 1-54 (1986). https://doi.org:10.1016/0301-0082(86)90019-5

42 Buzsaki, G. Theta oscillations in the hippocampus. *Neuron* **33**, 325-340 (2002). https://doi.org:10.1016/s0896-6273(02)00586-x

43 Sainsbury, R. S., Heynen, A. & Montoya, C. P. Behavioral correlates of hippocampal type 2 theta in the rat. *Physiol Behav* **39**, 513-519 (1987). https://doi.org:10.1016/0031-9384(87)90382-9

44 Sainsbury, R. S. Hippocampal theta: a sensory-inhibition theory of function. *Neurosci Biobehav Rev* **22**, 237-241 (1998). https://doi.org:10.1016/s0149-7634(97)00011-0

45 Barry, C., Heys, J. G. & Hasselmo, M. E. Possible role of acetylcholine in regulating spatial novelty effects on theta rhythm and grid cells. *Front Neural Circuits* **6**, 5 (2012). https://doi.org:10.3389/fncir.2012.00005

46 Nakajima, Y., Nakajima, S., Leonard, R. J. & Yamaguchi, K. Acetylcholine raises excitability by inhibiting the fast transient potassium current in cultured hippocampal neurons. *Proc Natl*

Acad Sci U S A **83**, 3022-3026 (1986). https://doi.org:10.1073/pnas.83.9.3022

47 Markram, H. & Segal, M. Acetylcholine potentiates responses to N-methyl-D-aspartate in the rat hippocampus. *Neurosci Lett* **113**, 62-65 (1990). https://doi.org:10.1016/0304-3940(90)90495-u

48 Fraser, D. D. & MacVicar, B. A. Cholinergic-dependent plateau potential in hippocampal CA1 pyramidal neurons. *J Neurosci* **16**, 4113-4128 (1996). https://doi.org:10.1523/JNEUROSCI.16-13-04113.1996

49 Toth, K., Freund, T. F. & Miles, R. Disinhibition of rat hippocampal pyramidal cells by GABAergic afferents from the septum. *J Physiol* **500 (Pt 2)**, 463-474 (1997). https://doi.org:10.1113/jphysiol.1997.sp022033

50 Colgin, L. L. Mechanisms and functions of theta rhythms. *Annu Rev Neurosci* **36**, 295-312 (2013). https://doi.org:10.1146/annurev-neuro-062012-170330

51 Cobb, S. R., Buhl, E. H., Halasy, K., Paulsen, O. & Somogyi, P. Synchronization of neuronal activity in hippocampus by individual GABAergic interneurons. *Nature* **378**, 75-78 (1995). https://doi.org:10.1038/378075a0

52 Stark, E. *et al.* Inhibition-induced theta resonance in cortical circuits. *Neuron* **80**, 1263-1276 (2013). https://doi.org:10.1016/j.neuron.2013.09.033

53 Landfield, P. W., McGaugh, J. L. & Tusa, R. J. Theta rhythm: a temporal correlate of memory storage processes in the rat. *Science* **175**, 87-89 (1972). https://doi.org:10.1126/science.175.4017.87

54 Berry, S. D. & Thompson, R. F. Prediction of learning rate from the hippocampal electroencephalogram. *Science* **200**, 1298-1300 (1978). https://doi.org:10.1126/science.663612

55 Belchior, H., Lopes-Dos-Santos, V., Tort, A. B. & Ribeiro, S. Increase in hippocampal theta oscillations during spatial decision making. *Hippocampus* **24**, 693-702 (2014). https://doi.org:10.1002/hipo.22260

56 Winson, J. Loss of hippocampal theta rhythm results in spatial memory deficit in the rat. *Science* **201**, 160-163 (1978). https://doi.org:10.1126/science.663646

57 Mitchell, S. J., Rawlins, J. N., Steward, O. & Olton, D. S. Medial septal area lesions disrupt theta rhythm and cholinergic staining in medial entorhinal cortex and produce impaired radial arm maze behavior in rats. *J Neurosci* **2**, 292-302 (1982). https://doi.org:10.1523/JNEUROSCI.02-03-00292.1982

58 Mizumori, S. J., Perez, G. M., Alvarado, M. C., Barnes, C. A. & McNaughton, B. L. Reversible inactivation of the medial septum differentially affects two forms of learning in rats. *Brain research* **528**, 12-20 (1990). https://doi.org:10.1016/0006-8993(90)90188-h

59 M'Harzi, M. & Jarrard, L. E. Effects of medial and lateral septal lesions on acquisition of a place and cue radial maze task. *Behav Brain Res* **49**, 159-165 (1992). https://doi.org:10.1016/s0166-4328(05)80160-3

60 Wang, Y., Romani, S., Lustig, B., Leonardo, A. & Pastalkova, E. Theta sequences are essential for internally generated hippocampal firing fields. *Nat Neurosci* **18**, 282-288 (2015). https://doi.org:10.1038/nn.3904

61 McNaughton, N., Ruan, M. & Woodnorth, M. A. Restoring theta-like rhythmicity in rats restores initial learning in the Morris water maze. *Hippocampus* **16**, 1102-1110 (2006). https://doi.org:10.1002/hipo.20235

62 Lee, D. J. *et al.* Medial septal nucleus theta frequency deep brain stimulation improves spatial working memory after traumatic brain injury. *J Neurotrauma* **30**, 131-139 (2013). https://doi.org:10.1089/neu.2012.2646

63 Hasselmo, M. E., Bodelon, C. & Wyble, B. P. A proposed function for hippocampal theta rhythm: separate phases of encoding and retrieval enhance reversal of prior learning. *Neural Comput* **14**, 793-817 (2002). https://doi.org:10.1162/089976602317318965

64 Rutishauser, U., Ross, I. B., Mamelak, A. N. & Schuman, E. M. Human memory strength is predicted by theta-frequency phase-locking of single neurons. *Nature* **464**, 903-907 (2010). https://doi.org:10.1038/nature08860

65 Siegle, J. H. & Wilson, M. A. Enhancement of encoding and retrieval functions through theta phase-specific manipulation of hippocampus. *Elife* **3**, e03061 (2014). https://doi.org:10.7554/eLife.03061

66 Vandecasteele, M. *et al.* Optogenetic activation of septal cholinergic neurons suppresses sharp wave ripples and enhances theta oscillations in the hippocampus. *Proc Natl Acad Sci U S A* **111**, 13535-13540 (2014). https://doi.org:10.1073/pnas.1411233111

67 Valero, M. *et al.* Determinants of different deep and superficial CA1 pyramidal cell dynamics during sharp-wave ripples. *Nat Neurosci* **18**, 1281-1290 (2015). https://doi.org:10.1038/nn.4074

68 Deuchars, J. & Thomson, A. M. CA1 pyramid-pyramid connections in rat hippocampus in vitro: dual intracellular recordings with biocytin filling. *Neuroscience* **74**, 1009-1018 (1996). https://doi.org:10.1016/0306-4522(96)00251-5

69 Caporale, N. & Dan, Y. Spike timing-dependent plasticity: a Hebbian learning rule. *Annu Rev Neurosci* **31**, 25-46 (2008). https://doi.org:10.1146/annurev.neuro.31.060407.125639

70 Markram, H., Lubke, J., Frotscher, M. & Sakmann, B. Regulation of synaptic efficacy by coincidence of postsynaptic APs and EPSPs. *Science* **275**, 213-215 (1997). https://doi.org:10.1126/science.275.5297.213

71 Bi, G. Q. & Poo, M. M. Synaptic modifications in cultured hippocampal neurons: dependence on spike timing, synaptic strength, and postsynaptic cell type. *J Neurosci* **18**, 10464-10472 (1998). https://doi.org:10.1523/JNEUROSCI.18-24-10464.1998

72 Ali, A. B., Deuchars, J., Pawelzik, H. & Thomson, A. M. CA1 pyramidal to basket and bistratified cell EPSPs: dual intracellular recordings in rat hippocampal slices. *J Physiol* **507 (Pt 1)**, 201-217 (1998). https://doi.org:10.1111/j.1469-7793.1998.201bu.x

73 Ali, A. B. & Thomson, A. M. Facilitating pyramid to horizontal oriens-alveus interneurone inputs: dual intracellular recordings in slices of rat hippocampus. *J Physiol* **507 (Pt 1)**, 185-199 (1998). https://doi.org:10.1111/j.1469-7793.1998.185bu.x

74 Engel, A. K., Konig, P., Kreiter, A. K. & Singer, W. Interhemispheric synchronization of oscillatory neuronal responses in cat visual cortex. *Science* **252**, 1177-1179 (1991). https://doi.org:10.1126/science.252.5009.1177

75 Alonso, J. M., Usrey, W. M. & Reid, R. C. Precisely correlated firing in cells of the lateral geniculate nucleus. *Nature* **383**, 815-819 (1996). https://doi.org:10.1038/383815a0

76 Zheng, Q. *et al.* Rational Design of Fluorogenic and Spontaneously Blinking Labels for Super-Resolution Imaging. *ACS Cent Sci* **5**, 1602-1613 (2019). https://doi.org:10.1021/acscentsci.9b00676

Acknowledgments

We express our sincere gratitude to Dr. Luke Lavis for sharing the JF_{552}-HaloTag ligand. Special thanks to Mr. Yu-Ting Lin and Ms. Hui-Ching Chen for technical assistance. We are grateful to Drs. Shih-Chieh Lin, Kuo-Hua Huang, Shi-Bing Yang, and Fu-Chin Liu for their insightful comments on the manuscript.

Funding statements

National Science and Technology Council, Taiwan (B.-J.L. and T.-W.C.)
Howard Hughes Medical Institute, USA (E.R.S.)

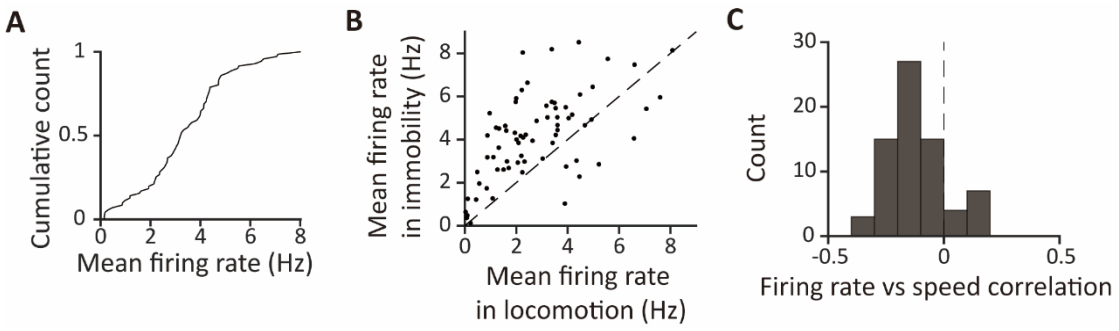

Supplementary Figure 1 Mean firing rate distribution and correlation with animals' speed.

(A) Cumulative distribution of mean firing rates averaged throughout the entire 180-second recording period.

(B) Mean firing rates during locomotion plotted against mean firing rates during immobility for individual cells. Each dot represents a cell. Mean firing rates are higher during immobility than during locomotion (4.2±0.2 Hz for immobility, 2.8±0.2 Hz for locomotion, n=71 cells, $p<0.001$, Wilcoxon signed-rank test).

(C) Histogram of correlation coefficients between instantaneous firing rates and the animals' speed for each neuron.

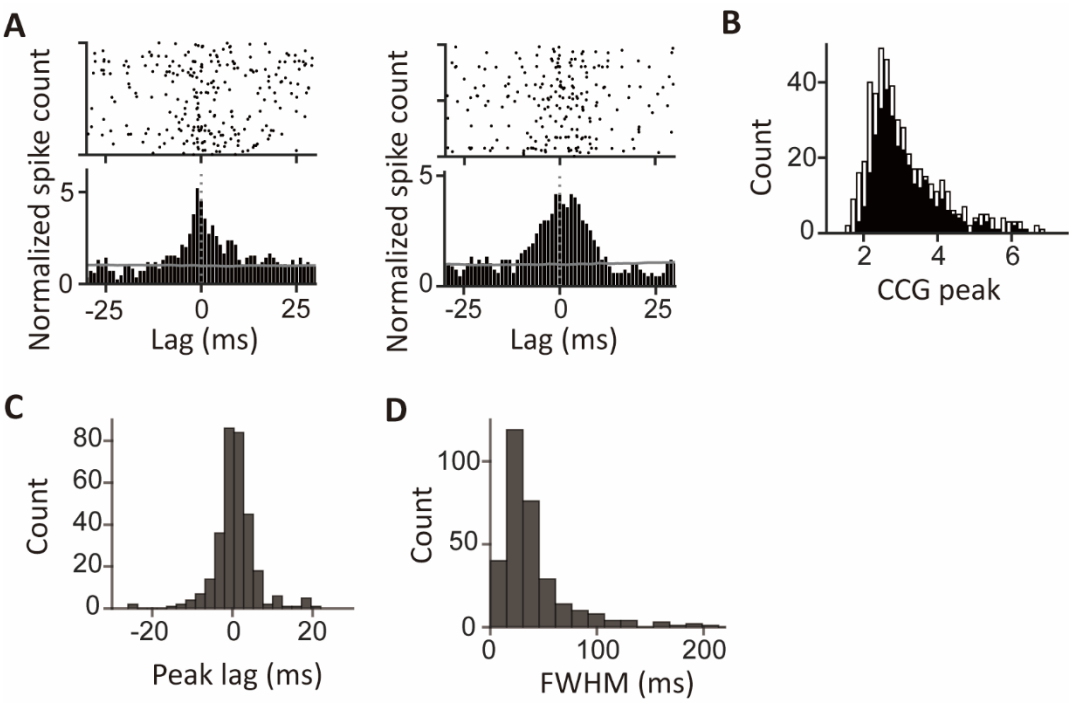

Supplementary Figure 2 Pairwise cross-correlogram (CCG) between CA1 pyramidal cells.

(A) CCGs of two representative cell pairs exhibiting significant peaks compared to the jittered spike trains of the target cells (gray lines).

(B) Distribution of the CCG peaks (n=497 pairs). Black: CCG peaks with significance ($p<0.05$). White: CCG peaks without significance ($p>=0.05$).

(C) Histogram of peak lags of significant CCG peaks (n=315 pairs).

(D) Histogram of FWHMs of significant CCG peaks (n=315 pairs).

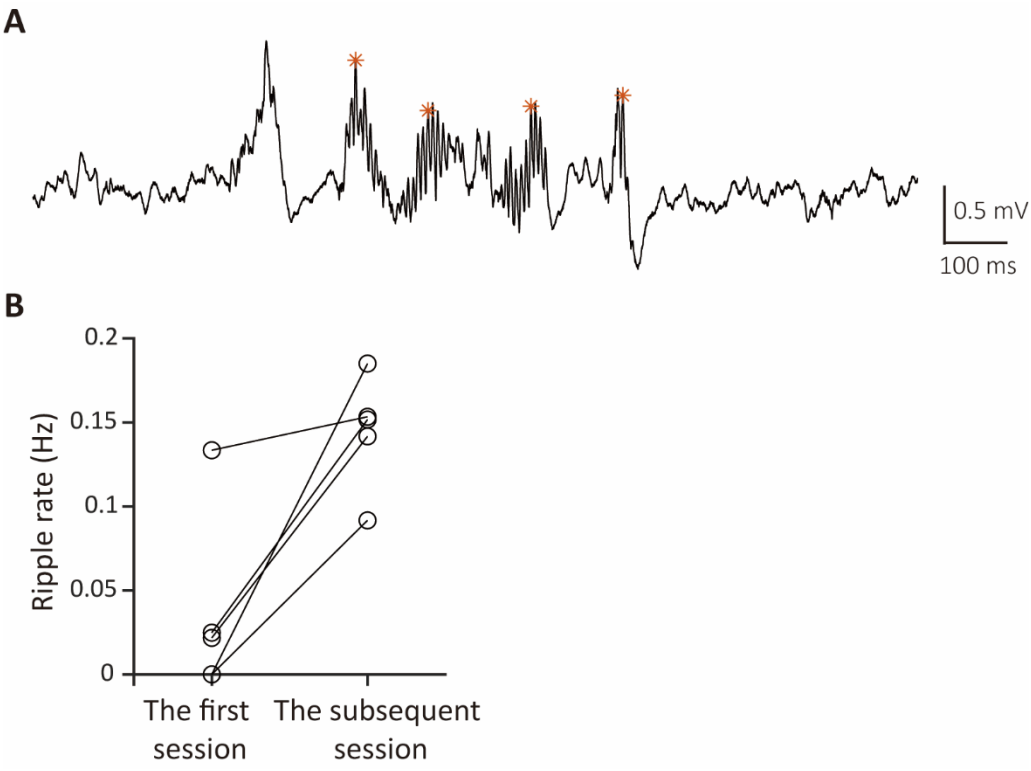

Supplementary Figure 3 LFP ripples recorded in the first and subsequent sessions in a novel maze. **(A)** An example LFP trace with ripples recorded in a subsequent session following the first session of novel exploration, where no ripple was detected.

(B) Ripple rates in the first and subsequent sessions recorded in the same animals (n=5 mice) during novel exploration.

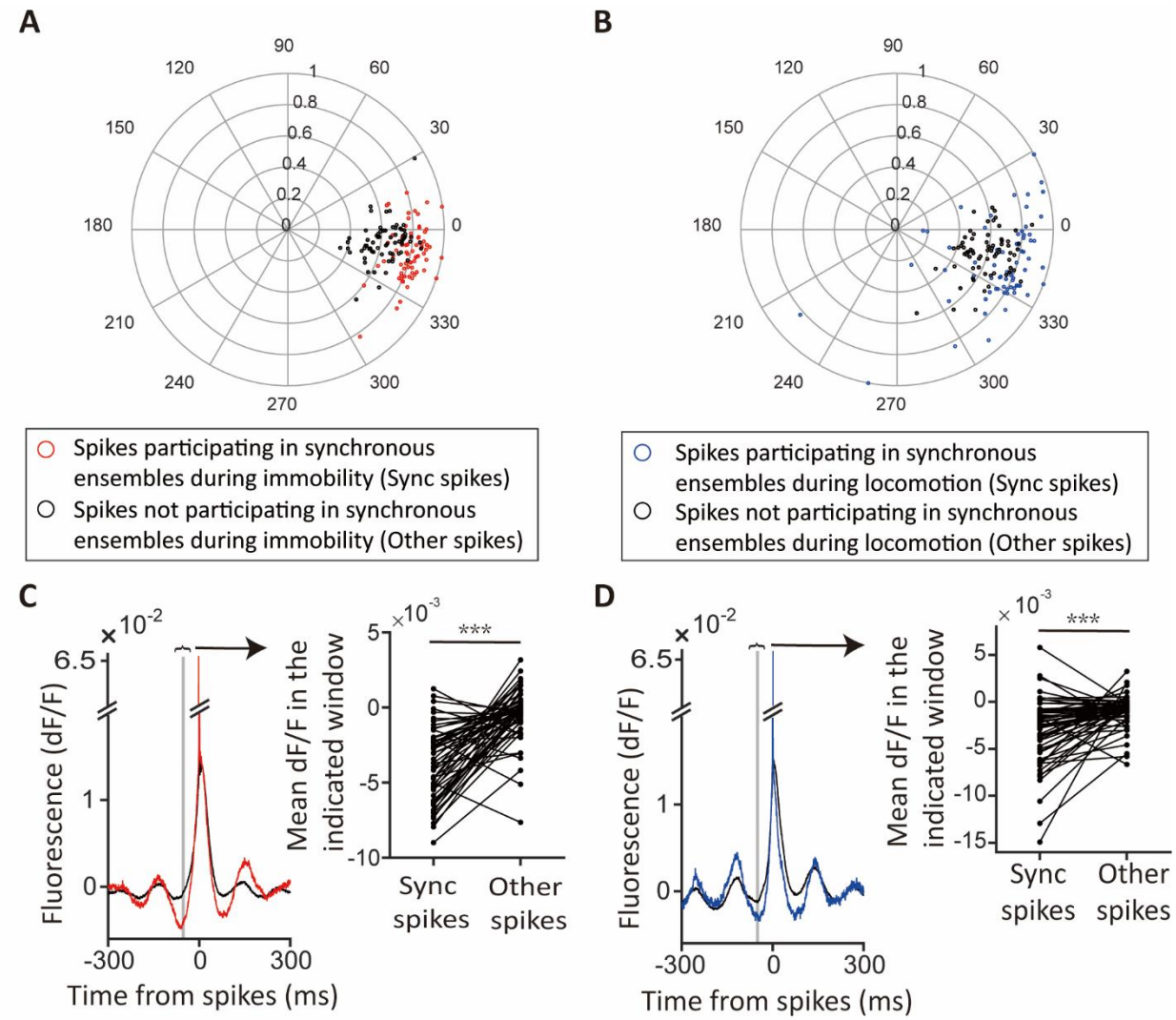

Supplementary Figure 4 Theta modulation of spikes during immobility and locomotion periods of novel exploration.

(A) Polar plot comparing theta modulation between spikes participating in synchronous ensembles (sync spikes) and spikes not participating in synchronous ensembles (other spikes) during immobility. Each dot represents the averaged modulation of a cell. The modulation strengths of spikes participating in synchrony are significantly higher than those of spikes not participating in synchrony (modulation strength for spikes participating in synchronous ensembles: 0.81±0.08, for spikes not participating in synchronous ensembles: 0.63±0.12, mean±s.d., n=71 cells, $p<0.001$, pair Student's *t*-test).

(B) Same as in (A), but during locomotion (modulation strength for spikes participating in

synchronous ensembles: 0.76±0.18, for spikes not participating in synchronous ensembles: 0.60± 0.12, mean±s.d., n=71 cells, $p<0.001$, pair Student's *t*-test).

(C) Average fluorescence triggered by cells' spikes participating in synchronous ensembles (red, sync spikes) and not participating in synchronous ensembles during immobility (black, other spikes; n=59 cells). Inset: Pairwise comparison of average fluorescence 50±5 ms before time of spikes (t=0) between the two triggered groups (n=59 cells).

(D) Same as in (C), but during locomotion.

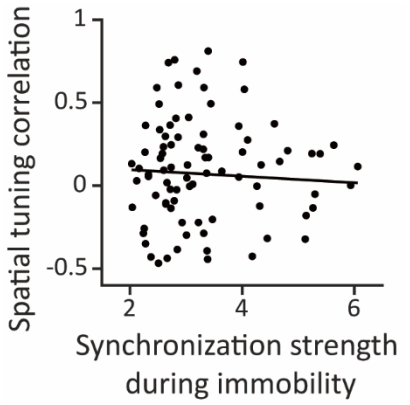

Supplementary Figure 5 Synchronization strengths during immobility show little correlation with the similarity of spatial tunings between place cells. Synchronization strengths during immobility plotted against correlation coefficients of spatial tunings for pairs of place cells. Synchronization strengths show little correlation with similarities of spatial tunings (Spearman correlation coefficient=-0.003, p=0.98, n=88 cell pairs).